buildings

MDPI

Article

Investigation of Process Parameters of Phosphogypsum for Preparing Calcium Sulfoaluminate Cement

Ping Zhang [1], Bingxin Zhang [1], Jun Chang [2,*], Tong Wang [2], Jixin Zhang [2] and Li Li [3]

[1] School of Materials and Architectural Engineering, Guizhou Normal University, Guiyang 550025, China
[2] School of Civil Engineering, Dalian University of Technology, Dalian 116024, China
[3] College of Water Resources and Architectural Engineering, Northwest A&F University, Xianyang 712100, China
* Correspondence: mlchang@dlut.edu.cn

Abstract: Preparing calcium sulfoaluminate cement (CAS) from solid waste phosphogypsum (PG) instead of natural gypsum is an effective way to utilize solid waste. In this paper, CAS clinker was successfully prepared from PG and the mineral content of calcium sulfoaluminate ($C_4A_3\overline{S}$) in the sample was above 65%. The effects of raw material ratio, calcination temperature, and time on clinker composition were investigated. The mechanical properties of different samples were tested. The optimum ratio for preparing CAS using PG was 42.23% limestone, 17.43% PG, and 40.34% bauxite. The optimal calcination conditions are a high temperature of 1250 °C for 45 min. The 3-day compressive strengths of the laboratory-prepared CAS were all above 50 MPa. It was found that as the calcination temperature increased, the amount of $C_4A_3\overline{S}$ produced gradually increased. Temperatures above 1300 °C resulted in the decomposition of $C_4A_3\overline{S}$. The calcination time did not significantly affect the mineral composition of the clinker or the strength of the cement. $C_4A_3\overline{S}$ was observed to be rounded and hexagonal platelets with crystal sizes of 1 to 2 μm, a relatively small size that is favorable to the hydration of $C_4A_3\overline{S}$, as observed by SEM images. In addition, the high calcination temperature affected the particle morphology of $C_4A_3\overline{S}$, changing it from a well-defined polygonal structure to a molten state. The test results provide helpful information for improving PG utilization and applying PG in CAS production.

Keywords: phosphogypsum; calcium sulfoaluminate cement; calcination temperature; calcination time; compressive strength

check for updates

Citation: Zhang, P.; Zhang, B.; Chang, J.; Wang, T.; Zhang, J.; Li, L. Investigation of Process Parameters of Phosphogypsum for Preparing Calcium Sulfoaluminate Cement. *Buildings* **2022**, *12*, 1774. https://doi.org/10.3390/buildings12111774

Academic Editor: Abdelhafid Khelidj

Received: 23 September 2022
Accepted: 18 October 2022
Published: 23 October 2022

Publisher's Note: MDPI stays neutral with regard to jurisdictional claims in published maps and institutional affiliations.

Copyright: © 2022 by the authors. Licensee MDPI, Basel, Switzerland. This article is an open access article distributed under the terms and conditions of the Creative Commons Attribution (CC BY) license (https://creativecommons.org/licenses/by/4.0/).

1. Introduction

Phosphogypsum (PG), consisting of calcium sulfate dihydrate and some impurities (sulfuric acid, phosphoric acid, phosphide, fluoride, and organic matter), is a solid waste from the wet phosphoric acid process [1,2]. Due to the development of the phosphate industry, PG emissions are increasing. Annual PG emissions worldwide are 280 million tonnes, of which China emits about 80 million tonnes annually [3]. No practical method has been found to treat PG, and less than 10% of it is used to prepare ammonium sulfate, soil modifiers, gypsum gelling materials, or silicate cement retarders [4–6]. Untreated PG exists in large piles on vacant land, which not only occupies land, but pollutes the ecological environment, poses a significant safety hazard, and restricts the development of the phosphate industry [7,8]. Therefore, the question to be addressed is how to deal with PG.

Calcium sulfoaluminate cement (CAS) is a hydraulic gel material with excellent properties such as fast hardening, early strength, low alkalinity, frost resistance, seepage resistance, and corrosion resistance. CAS is made by mixing a certain proportion of gypsum, bauxite, and limestone as raw materials, calcining at a high temperature to form a clinker with calcium sulfoaluminate ($C_4A_3\overline{S}$) and dicalcium silicate (C_2S) as the primary minerals, and then adding an appropriate proportion of gypsum [9–11]. CAS has a low lime saturation factor

and requires less limestone to prepare the raw material for cement, so it emits relatively less carbon dioxide [12–14]. In addition, the calcination temperature of sulfate aluminate cement clinker is about 150 °C lower than that of ordinary silicate cement clinker [15–17], and the fuel consumed during calcination is lower, making calcium sulfoaluminate cement a low-consumption and low-carbon-emission cementitious material that is of increasing interest to companies and researchers [18,19].

Currently, China has many PG emissions and large stockpiles, and there is a huge potential problem of environmental pollution [20]. Moreover, with the rapid development of urban and rural construction, the demand for special cement is also increasing [21,22]. The content of gypsum dihydrate in PG is above 85%, similar to the main component of natural gypsum [23]. The use of PG to replace natural gypsum in the preparation of CAS has become a popular topic for research [24], and it is essential to improve the utilization rate of PG and reduce the cost of CAS cement. However, few comparative investigations exist on the preparation of sulfate aluminate cement from PG.

Shen et al. successfully produced belite sulfoaluminate-ternesite cement in the laboratory using PG by secondary heat treatment with low early hydration strength [25]. Huang et al. investigated the effects of impurities of phosphoric acid, dicalcium phosphate, and calcium phosphate on CAS. The results showed that phosphoric acid and phosphate adversely affected CAS's hydration and mechanical properties, with phosphoric acid having the most significant effect [26]. Zhao et al. used density functional theory (DFT) simulations to demonstrate that P atoms were more likely to replace S atoms to form phosphorus-doped ye'elimite when PG was used to produce CAS clinker [27]. Previous studies have focused on the hydration of PG-prepared CAS clinker's hydration characteristics, properties, and doping mechanism [28–30]. However, no systematic research has been conducted on the preparation process of CAS produced by PG, which is of great importance for industrial production.

This study prepared CAS clinker from PG, bauxite, and limestone by controlling the process parameters. The mineral composition and compressive hydration strength of CAS clinker were studied under different conditions to obtain the optimal preparation process. Various raw materials ratios were calculated based on their composition and calcined to obtain CAS clinker with different mineral compositions. The optimum ratio of raw materials was determined by analyzing the clinker mineral composition and cement compressive strength. The clinker calcination process was optimized by controlling the calcination temperature and time. The optimum calcination conditions were determined according to the composition of the clinker minerals and the tested mechanical properties. A dosage scheme and process parameter model for CAS cement clinker with PG was established as the primary raw material.

2. Experimental Protocol

2.1. Raw Materials

This paper's bauxite, PG, and limestone were all sourced from Guizhou Urnford Group. All raw materials were ground by a planetary ball mill and passed through an 80 μm square hole sieve with less than a 5% residue rate. The chemical composition of the raw materials is listed in Table 1, and the X-ray diffractometer (XRD) analysis of PG, bauxite, and limestone is shown in Figure 1. The XRD pattern shows that the main mineral phases of PG are gypsum dihydrate and quartz. The main mineral phases of limestone are calcite and dolomite, and the primary mineral phases of bauxite are alumina, quartz, and hematite.

Table 1. Chemical compositions of the materials (wt.%).

Materials	SO_3	CaO	SiO_2	Al_2O_3	Fe_2O_3	TiO_2	MgO	P_2O_5	F	LOI
PG	50.33	39.78	3.61	0.28	0.37	0.08	-	0.83	0.67	4.05
Limestone	0.16	88.68	3.55	0.94	0.71	-	4.39	-	-	1.57
Bauxite	5.80	0.45	9.60	69.56	4.74	5.47	0.18	-	-	4.2

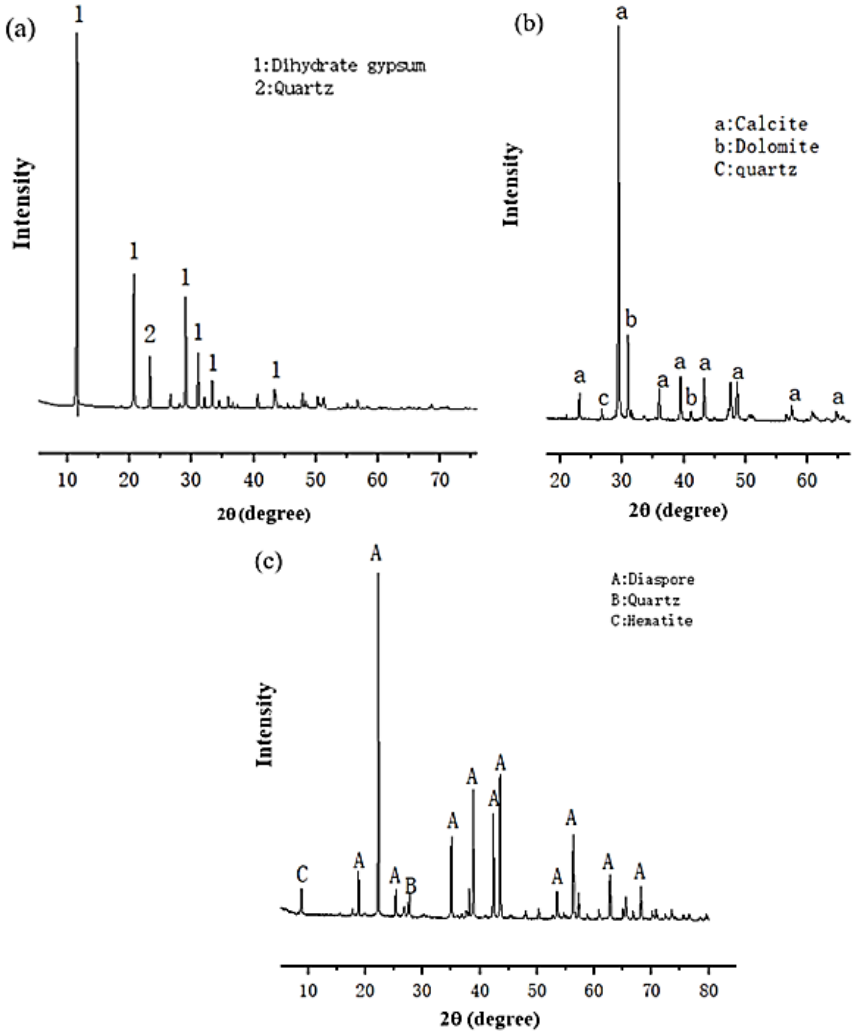

Figure 1. XRD patterns of materials: (**a**) PG, (**b**) limestone, (**c**) bauxite.

Figure 2 shows the particle size distribution profile of the three raw materials after grinding. The finer the raw material, the larger the specific surface area, and the faster the raw material reacts to produce clinker minerals during calcination. Therefore, the particle size of the three raw materials was measured using a laser diffraction particle size analyzer (NKT6200, Jinan, China). As shown in Figure 2, the particle size distribution of PG is more concentrated, mainly around 70 μm. In contrast, the particle size distribution of bauxite and limestone is broader, but the fineness of all three raw materials is controlled to pass through an 80 μm square hole sieve with a sieve margin of less than 5%. The target phase combinations for CAS clinker are shown in Table 2. Based on the target phase combinations and the chemical composition in Table 1, the ratios for CSA cement raw materials were determined, as shown in Table 3. The ground raw materials were accurately weighed and homogenized according to the ratios in Table 3. The raw material mixture was mixed with 10 wt.% water and pressure molded. After drying in a 40 °C oven, it was placed in a high-temperature furnace for firing. The firing process is shown in Figure 3. After calcination, the clinker was removed for rapid cooling. The samples were cooled and placed in a planetary ball mill for 5 min, and then ground finely in an agate mortar to pass through an 80 μm sieve. Analytical tests were carried out to determine the optimum raw material ratio, different calcination processes were used to prepare the cement clinker, and the effect of calcination temperature and time on the minerals and compressive strength of the cement clinker was investigated. The calcination conditions for different samples are shown in Table 4.

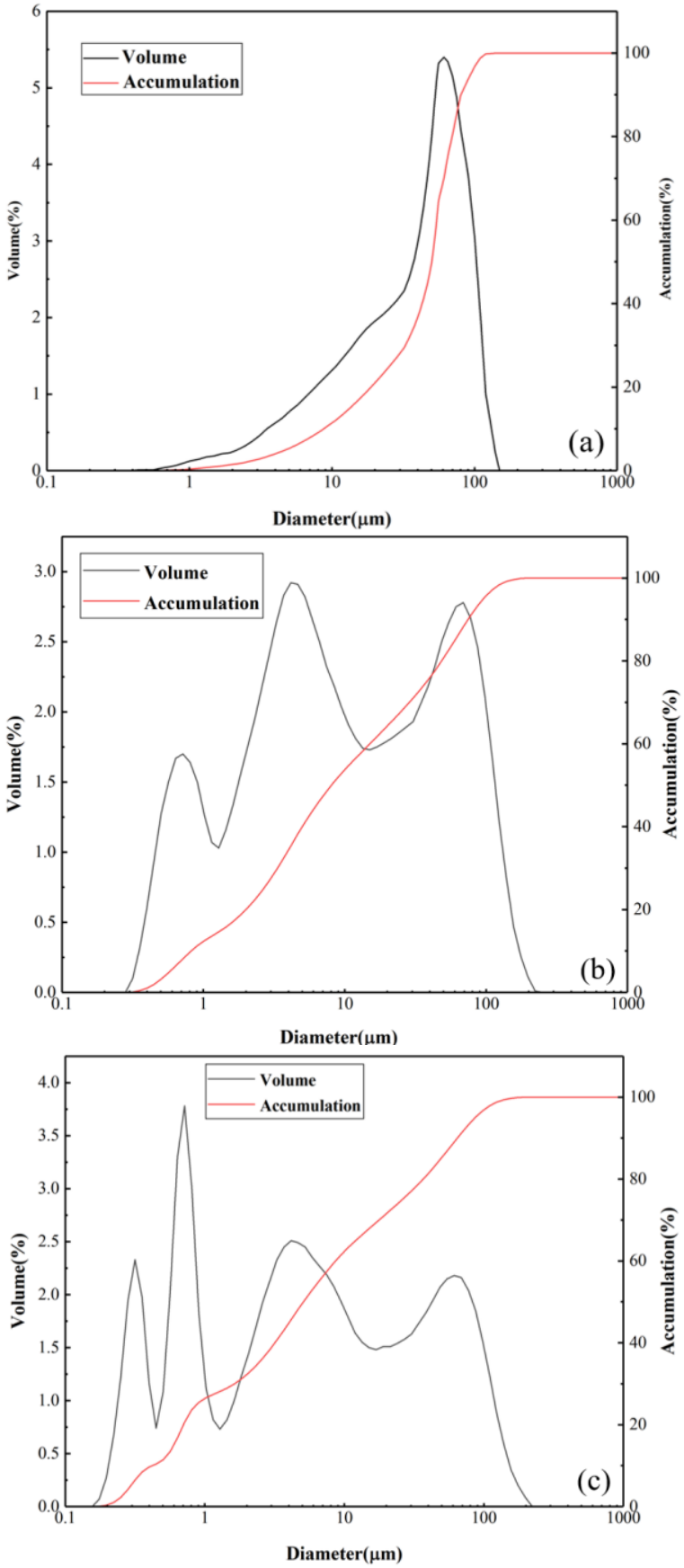

Figure 2. Particle size distribution of materials: (**a**) PG, (**b**) limestone, (**c**) bauxite.

Table 2. Design mineral composition of cement clinker (wt.%).

Sample	$C_4A_3\overline{S}$	C_4AF	C_2S	$C\overline{S}$
S1	74	8	18	0
S2	69	8	18	5
S3	64	8	18	10
S4	59	8	18	15

Table 3. Proportioning of the cement raw materials (wt.%).

Sample	Limestone	Phosphogypsum	Bauxite
S1	45.28	12.15	42.57
S2	42.23	17.43	40.34
S3	39.44	22.67	37.89
S4	37.23	27.32	35.45

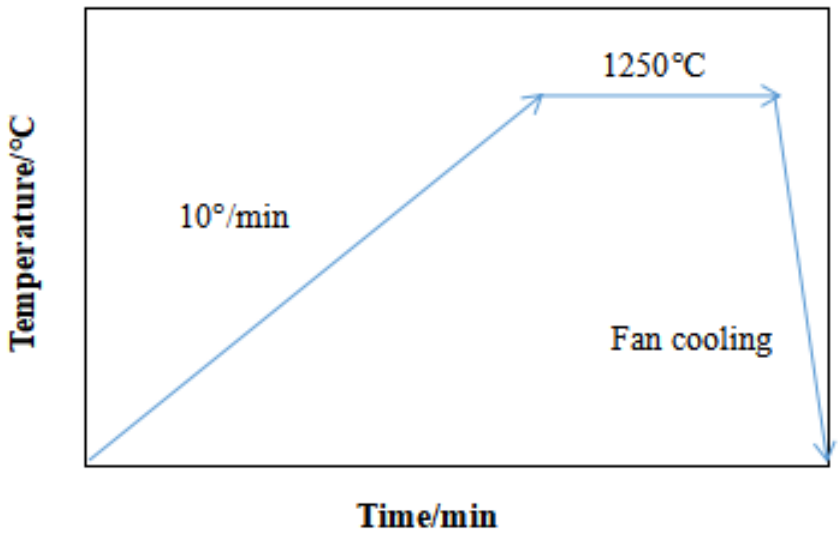

Figure 3. Cement clinker firing process.

Table 4. Calcination conditions of samples.

Sample	Calcination Temperature	Calcination Time
T1	1150 °C	45 min
T2	1200 °C	45 min
T3	1250 °C	45 min
T4	1300 °C	45 min
D1	1250 °C	30 min
D2	1250 °C	45 min
D3	1250 °C	60 min
D4	1250 °C	75 min

2.2. Test Methods

The thermal gravimetric (TG) tests were carried out using an integrated heat analyzer (Mettler-Toledo TGA/DSC1, Switzerland) in a dry nitrogen environment at 50 mL/min. The dried raw materials were ground into powders with a diameter of less than 80 μm, mixed homogeneously according to the ratios shown in Table 3 and placed in an alumina crucible, and ramped up from 50 to 1300 °C at a rate of 10 °C/min. The DTG curve was obtained by solving the TG curve in the first order. The DTG curve reflects the decomposition peaks corresponding to the decomposition of the different phases.

The calcined cement clinker was ground and passed through an 80 μm sieve for XRD (Bruker D8 Advance, German) analysis. The instrument emission light source was a copper

target (λ = 0.154 nm) with an operating voltage of 40 kV and an operating current of 40 mA. The test range was 5–80° (2θ) with a single step scan time of 0.5 s at a step size of 0.02°. The XRD profiles were first qualitatively analyzed using EVA software to determine the type of physical phase of the samples to be tested. This was followed by a quantitative analysis of the clinker mineral composition of the different samples by the Rietveld method (error 2%) using TOPAS 4.2 software [31]. The parameters fitted during the quantitative analysis were the background coefficient, zero displacement error, phase scale, cell parameters, phase shape parameters, and the merit orientation factor [32]. Due to a large amount of amorphous material in the cement samples, the tests were performed using the standard internal method, where 15 wt.% ZnO was added to the samples as an internal standard to determine the amount of ACn (containing amorphous phases, which are poorly crystallized and undetected by XRD) [33,34]. The Rietveld refinement process uses the Rwp value as an evaluation indicator for the fit results' reliability; usually, when Rwp < 15%, the results are considered reliable [35–37].

CAS clinker and gypsum dihydrate were mixed and ground at a molar ratio of 1:1.5 to obtain CAS cement, which was poured into a mixer at a water–cement ratio of 0.5 and mixed for two minutes at a controlled speed of 110–120 r/min to obtain a net cement paste. Cubic specimens were prepared using a 20 mm × 20 mm × 20 mm mold, initially placed at a temperature of (20 ± 1) °C and (95 ± 1)% humidity in a standard conditioning room. After demolding, the cubic specimens were cured in a standard curing chamber. The test cubes were tested for compressive strength using a microcomputer-controlled electronic universal testing machine (WDW-50, China). All test results were averaged from three sets of tests, and provide the characteristic values of compressive strength with standard deviation.

The microstructure of the cement clinker samples was observed by scanning electron microscopy (FEI NOVA Nano-SEM 450, USA). The accelerating voltage was 3 or 6 kV, and the electron beam's spot size was 3.0. The samples were gold coated for 30 s and then placed in the instrument for testing.

3. Results and Discussion

3.1. Thermal Analysis

Figure 4 shows the thermal analysis curves of cement raw materials at different ratios. As shown in Figure 4a, there are several weight loss peaks in the thermogravimetric curve. The first weight loss peak occurs at 150–170 °C; mainly, the raw material undergoes a dehydration reaction, including physical and crystalline water. The second corresponding weight loss peak occurs at 490–510 °C, mainly when the bauxite undergoes a decomposition reaction, forming Al_2O_3 and SiO_2. The third occurs at 700–800 °C, where the decomposition reaction of limestone occurs at this stage, producing CaO and CO_2, reacting as in Equation (1) [29]. The last occurs at 900 to 1030 °C and is due to the decomposition of PG, as shown in Equation (2) [38,39].

$$CaCO_3 \rightarrow CaO + CO_2 \uparrow \quad (1)$$

$$2CaSO_4 \rightarrow 2CaO + 2SO_2 \uparrow + O_2 \uparrow \quad (2)$$

$$2CaO + Al_2O_3 + SiO_2 \rightarrow 2CaO \cdot Al_2O_3 \cdot SiO_2 \quad (3)$$

$$3CaO + 3Al_2O_3 + CaSO_4 \rightarrow 3CaO \cdot 3Al_2O_3 \cdot CaSO_4 \quad (4)$$

$$3CaO + 3(2CaO \cdot Al_2O_3 \cdot SiO_2) + CaSO_4 \rightarrow 3CaO \cdot 3Al_2O_3 \cdot CaSO_4 + 3(2CaO \cdot SiO_2) \quad (5)$$

$$2CaO + SiO_2 \rightarrow 2CaO \cdot SiO_2 \quad (6)$$

$$2(2CaO \cdot SiO_2) + CaSO_4 \rightarrow 4CaO \cdot 2SiO_2 \cdot CaSO_4 \quad (7)$$

$$4CaO \cdot 2SiO_2 \cdot CaSO_4 \rightarrow 2(2CaO \cdot SiO_2) + CaSO_4 \quad (8)$$

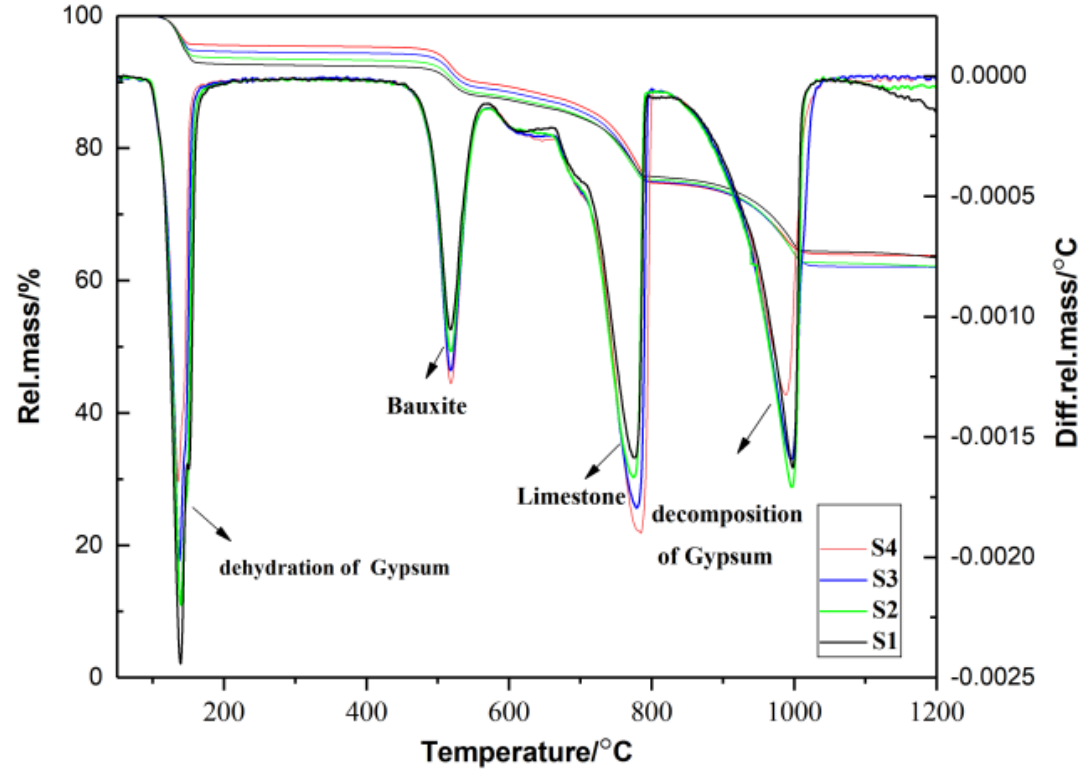

(**a**)

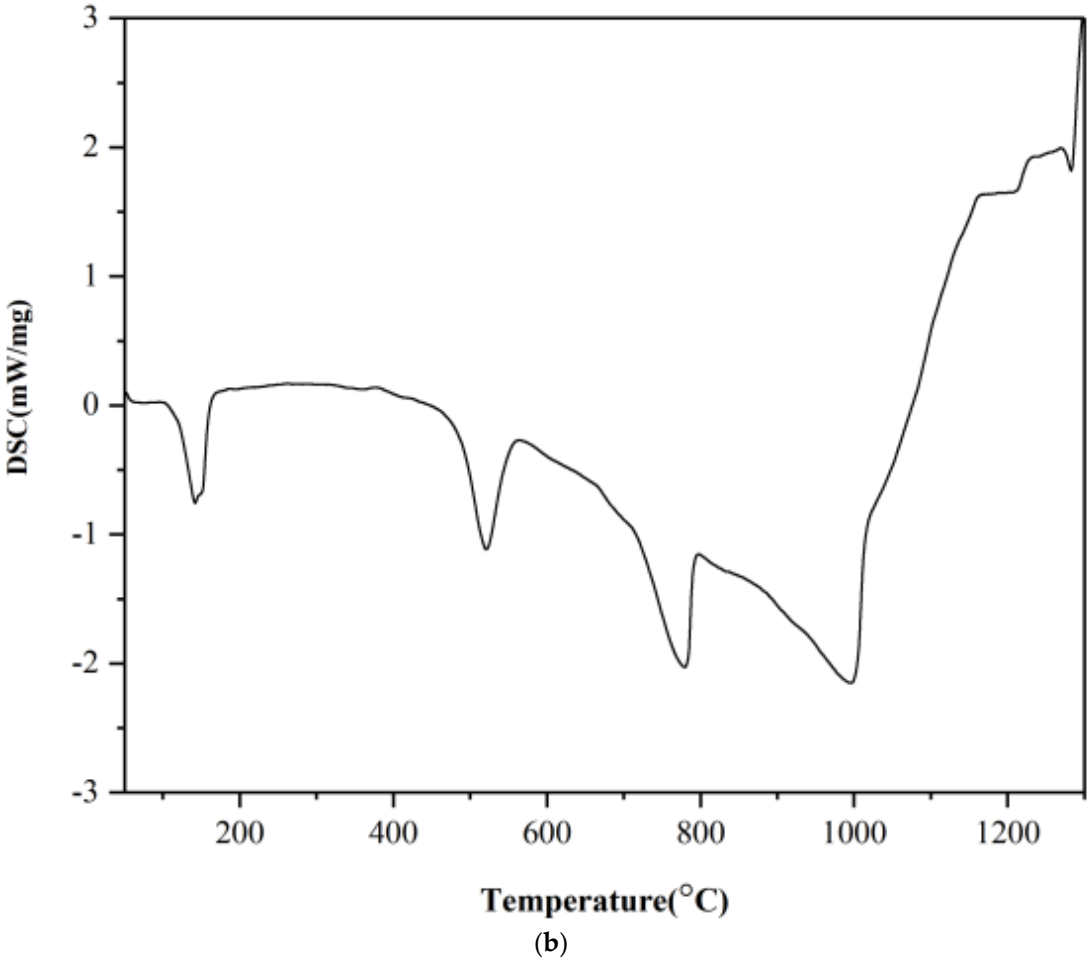

(**b**)

Figure 4. Thermal analysis curves for cement raw meal: (**a**) TG−DTG. (**b**) DSC.

As the temperature continues to rise, 2CaO-Al_2O_3-SiO_2 begins to form, and when it increases to 1000 °C, $C_4A_3\overline{S}$ and C_2S gradually develop, and the main chemical reactions that occur during the formation process are shown in Equations (3)–(8) [18,40]. Therefore, the comprehensive reaction process above is divided into three main stages. First is the stage of dehydration and decomposition of raw materials. The second is the generation stage of the intermediate mineral phase, mainly including intermediate products such as C_2AS and CA. The final stage is the generation stage of $C_4A_3\overline{S}$, which is primarily the reaction between the intermediate mineral phases. The thermal analysis of the cement raw meal indicated that the cement clinker was produced at a temperature of 1100 to 1300 °C. Based on this analysis, the next section of the raw meal was prepared by continuous calcination at 1250 °C for 60 min, which also provided a reference basis for further determination of the optimum calcination process.

3.2. Determination of CAS Raw Material Ratios

3.2.1. Clinker Mineral Composition Analysis

Figure 5 shows the XRD patterns of the cement clinker with different ratios. XRD curves have distinctive peaks characteristic of the homogenous minerals, mainly $C_4A_3\overline{S}$, C_2S, C_2AS, and $C\overline{S}$. From S1 to S4, the diffraction peaks of $C_4A_3\overline{S}$ in the prepared cement clinker gradually decrease as the $C_4A_3\overline{S}$ content in the design solution decreases. Quantitative analysis of the cement clinker minerals was carried out to determine the content of each phase in the clinker. The results of the Rietveld quantitative analysis are shown in Table 5. The $C_4A_3\overline{S}$ content was high in all four groups of samples and exceeded 65%, with the highest content reaching 76.68%. The crystalline structure of $C_4A_3\overline{S}$ is a porous skeleton consisting of connected aluminum-oxygen tetrahedra, which are highly reactive due to their porous structure and can be rapidly hydrated in the presence of gypsum generating ettringite (AFt), thus improving its early compressive strength [41–43]. It is therefore hypothesized that adding a certain amount of gypsum dihydrate to the four groups of cement clinker will result in a high content of calcium sulfoaluminate, leading to faster development of cement strength and higher early strength in all cases. C_2S and $C\overline{S}$ in the clinker are lower than the design value. Due to the decomposition of PG during calcination, the actual residual amount of calcium sulfate is less than the design value. Analyzing the results of the S1 group of tests, there is no residual $C\overline{S}$ in the design scenario, which exactly meets the demand for $C_4A_3\overline{S}$ mineral production. However, it can be seen from the quantitative results that when the PG decomposed, the remaining $C\overline{S}$ could not meet the need for the conversion of 2CaO-Al_2O_3-SiO_2 (C_2AS) to $C_4A_3\overline{S}$ and C_2S, resulting in the clinker minerals containing the intermediate mineral C_2AS. Thus, the C_2S and $C\overline{S}$ content in each group of clinker minerals was less than the design amount, and the extra PG dispensed into the raw meal was converted to high-temperature hard gypsum. It can also be seen that the C_2S content in the S1–S4 samples gradually increases. Under the presence of gypsum, the rate of hydration of C_2S develops slowly and gradually increases in the later stages. Therefore, it can be assumed from this that the compressive strength of S4 develops relatively well in the later stages compared to S1.

Table 5. Contents of cement clinker minerals (wt.%).

Sample	Phase Content (wt.%)					R_{wp} (%)
	$C_4A_3\overline{S}$	C_2S	C_4AF	$C\overline{S}$	C_2AS	
S1	76.68	10.30	3.24	-	9.78	12.17
S2	76.00	12.55	3.95	2.29	5.21	11.40
S3	73.00	13.54	5.42	5.26	2.78	12.76
S4	66.67	15.81	3.98	10.80	2.74	12.33

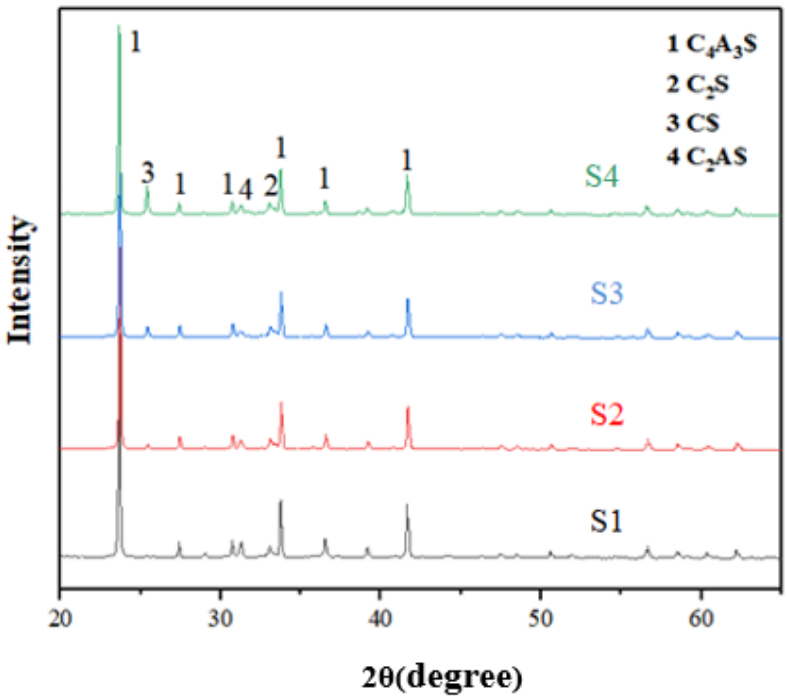

Figure 5. XRD patterns of different samples at 1250 °C for 60 min.

The microscopic morphology of Group S2 cement clinker was analyzed by SEM photographs, as shown in Figure 6. It can be seen from the photographs that the clinker is mostly calcium sulfate aluminate minerals with crystal sizes of about 1 to 2 μm, in the form of hexagonal plates or fine rounded crystals with smooth surfaces, and closely arranged with uniform sizes between the particles. A large amount of $C_4A_3\overline{S}$ can react quickly to produce ettringite (AFt) during hydration, which causes the cement test block to obtain high early compressive strength.

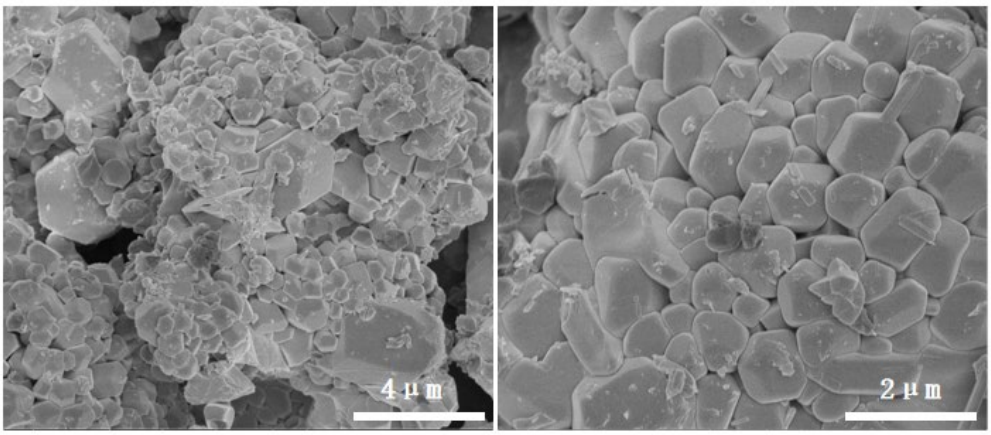

Figure 6. SEM micromorphology of cement clinkers.

3.2.2. Compressive Strength

Figure 7 shows the compressive strength of the cement test blocks for four different ratios. It can be seen from the figure that the early compressive strength follows the same trend as the content of $C_4A_3\overline{S}$ minerals in the samples and decreases with the decrease in $C_4A_3\overline{S}$ minerals. The early strength of the four groups of samples mainly originates from the hydration of $C_4A_3\overline{S}$ and the generation of AFt. At 1 day of age, S1 had the highest compressive strength of 44.8 MPa, and S4 had the lowest compressive strength of 40 MPa. After 3 days of hydration, S2 had the highest compressive strength of 55.5 MPa,

followed by S1 at 54.2 MPa. The late compressive strength development of the samples was relatively slow, probably because of the low C_2S mineral content. In summary, the S2 specimens showed the best strength development and did not show strength inversion at the later stage.

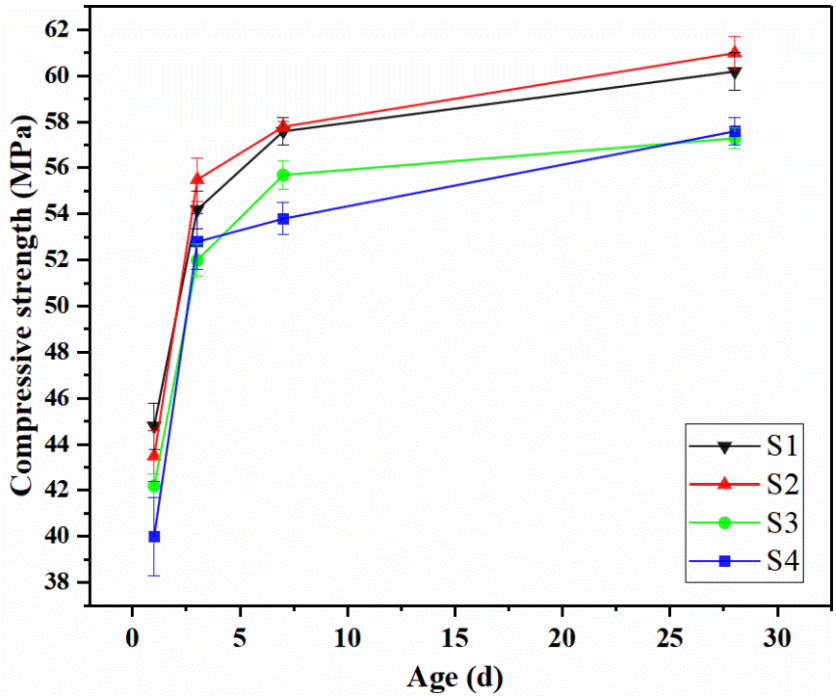

Figure 7. Compressive strength of cement with different proportions.

Combined with the mineral composition, the $C_4A_3\overline{S}$ content is high, and thus the hydration activity is good. Through the rapid hydration of $C_4A_3\overline{S}$ with hard gypsum in the early stages of hydration, it has good early compressive strength, reaching 44.8 MPa at 1 d. In this test, S2 can be chosen as the best mix ratio design, and the effect of different calcination processes on the clinker was determined later. In addition to this, when looking at the compressive strength of the test blocks in group S4, although the compressive strength was lower than that of the other three groups, the compressive strength grew fastest in the later stages, which verifies that group S4 had the highest C_2S content in the cement clinker and the fastest growth in compressive strength in the later stages when the cement clinker was quantified.

3.3. Calcination Process Optimisation

3.3.1. Calcination Temperature

Figure 8 shows the XRD patterns of the S2 samples at different calcination temperatures. The diffraction peaks of $C\overline{S}$ and C_2AS are obvious at 1150 °C, and the diffraction peak of $C_4A_3\overline{S}$ is relatively weak, so it can be seen that the firing process has not been entirely completed. There are still transitional phases of C_2AS and $C\overline{S}$ in the clinker, which has not been completely transformed into $C_4A_3\overline{S}$ and C_2S. Accordingly, the transitional phases in the cement clinker can be used to determine the calcination temperature of the clinker and to judge whether the clinker reaction process is completed. When the calcination temperature rises from 1150 to 1250 °C, the diffraction peak of $C_4A_3\overline{S}$ gradually increases, and when the calcination temperature continues to grow to 1300 °C, the diffraction peak of $C_4A_3\overline{S}$ decreases. According to this, it can be seen that when the temperature rises to 1300 °C, $C_4A_3\overline{S}$ begins to decompose, and the reaction equation is shown in Equations (9) and (10) [44]. An observation of the clinker will show that the clinker center produces molten lumps with a

yellow-brown color, indicating that the calcination temperature is high. Figure 9 shows the pictures of experimental samples before and after high-temperature calcination.

$$2(4CaO \cdot 3Al_2O_3 \cdot SO_3) \rightarrow 6(CaO \cdot Al_2O_3) + 2CaO + 2SO_2 \uparrow + O_2 \uparrow \quad (9)$$

$$10(4CaO \cdot 3Al_2O_3 \cdot SO_3) \rightarrow 16(CaO \cdot Al_2O_3) + 2(12CaO \cdot 7Al_2O_3) + 10SO_2 \uparrow + 5O_2 \uparrow \quad (10)$$

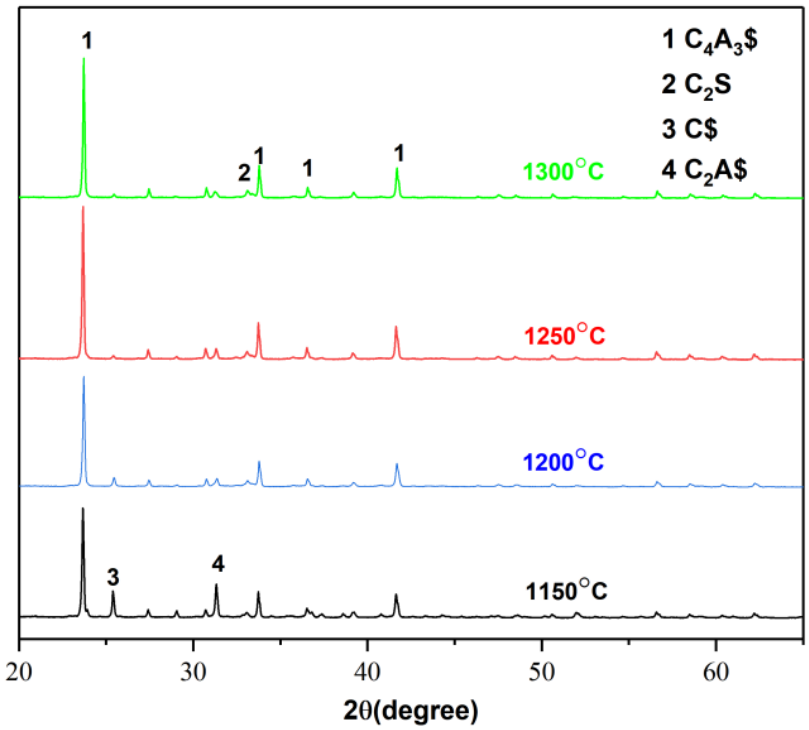

Figure 8. XRD patterns of S2 samples fired at different temperatures.



Figure 9. Preparation of CAS clinker by high temperature calcination.

The mineral content of the S2 samples at different calcination temperatures shown in Table 6 was quantified by the Rietveld method. At a calcination temperature of 1150 °C, the clinker contains less $C_4A_3\overline{S}$ at 58.67%, while it contains 14.45% C_2AS and 8.34% $C\overline{S}$, indicating that the calcination temperature is insufficient and the reaction is not complete. As the temperature increased, the $C_4A_3\overline{S}$ content gradually increased, and the intermediate mineral C_2AS disappeared. When the temperature rose to 1300 °C, the $C_4A_3\overline{S}$ content dropped to 68.56%, while a small amount of $C_{12}A_7$ and CA appeared in the clinker when the temperature was too high, and $C_4A_3\overline{S}$ decomposed. Therefore, the calcination temperature

of CAS clinker was determined to be 1250 °C to ensure the adequate formation of clinker minerals and prevent over-burning.

Table 6. Contents of S2 samples fired at different temperatures (wt.%).

Sample	Phase Content (wt.%)							R_{wp} (%)
	$C_4A_3\bar{S}$	C_2S	C_4AF	$C\bar{S}$	C_2AS	$C_{12}A_7$	CA	
T1	58.67	13.30	5.24	8.34	14.45	-	-	9.15
T2	67.34	14.53	4.97	5.78	7.38	-	-	11.78
T3	72.89	15.48	5.62	3.72	2.29	-	-	10.40
T4	68.56	14.81	5.15	2.45	-	3.25	5.78	12.11

The compressive strength of CAS at different calcination temperatures is shown in Figure 10. When the calcination temperature is increased from 1150 to 1250 °C, the compressive strength of the cement shows an increasing trend with increasing calcination temperature. In contrast, when the calcination temperature rises to 1300 °C, the cement's compressive strength decreases slightly, which is related to the clinker's mineral composition. The cement compressive strength is in good agreement with the XRD analysis, and the calcination temperature of 1250 °C was chosen for the firing of the clinker.

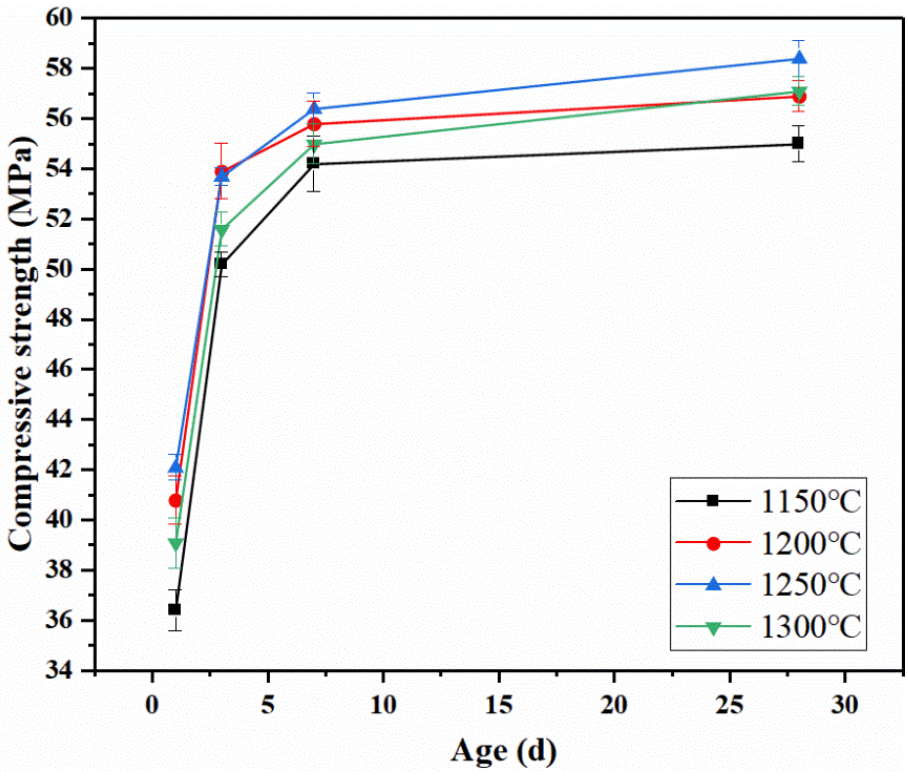

Figure 10. Compressive strength of cement at different firing temperatures.

Figure 11 shows the microscopic morphology of S2 at different calcination temperatures. Comparing Figure 11a–c, it is found that the morphological characteristics of $C_4A_3\bar{S}$ are the same when the calcination temperature is 1150 to 1250 °C. The size of the fired $C_4A_3\bar{S}$ particles are about 1 to 2 μm, with a polygonal structure and precise outline, and the inter-particle boundary is clear. When the temperature was increased to 1300 °C, the morphological characteristics of the particles in Figure 11d show that most of the $C_4A_3\bar{S}$ particles had no apparent outline shape, and the particles were fused without obvious boundaries. Therefore, when the calcination temperature is too high, it will affect the particle morphology of $C_4A_3\bar{S}$, and changing it from a well-defined polygonal structure to a molten state will affect the cement's hydration reaction.

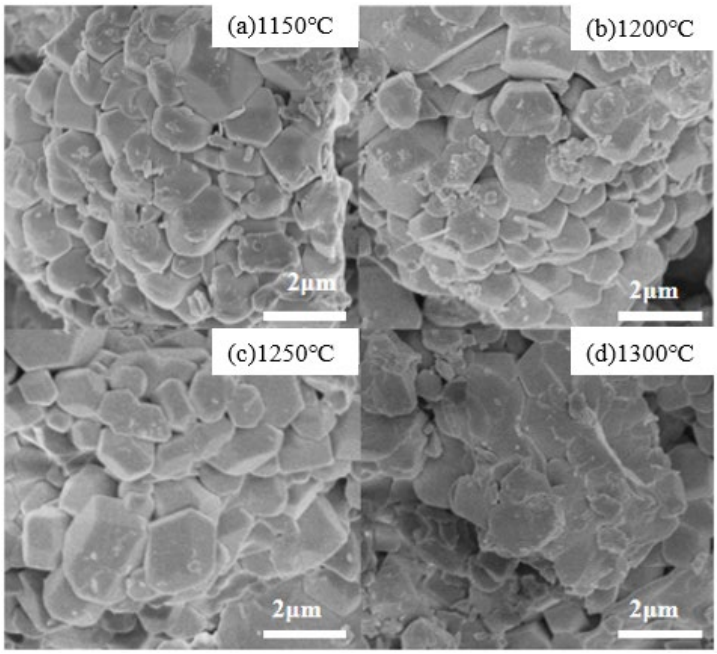

Figure 11. SEM micromorphology of S2 samples at different calcination temperatures.

3.3.2. Calcination Time

Figure 12 shows the XRD patterns of the S2 sample calcined at 1250 °C at different times. It can be seen from the graph that the intensity of the diffraction peaks of $C_4A_3\overline{S}$ increased when the calcination time was increased from 30 to 45 min, indicating that the increase in time favored the formation of clinker minerals. The increase in time from 45 to 75 min did not result in any significant change in the diffraction peaks of the cement clinker minerals, indicating that calcination time within this range did not significantly affect mineral formation. It can be assumed that the clinker minerals were already formed after 45 min of calcination at a high temperature, and there was no need to extend the calcination time further. Therefore, in terms of the mineral composition of the cement clinker, 45 min can be chosen as the optimum time for the calcination of the CAS clinker.

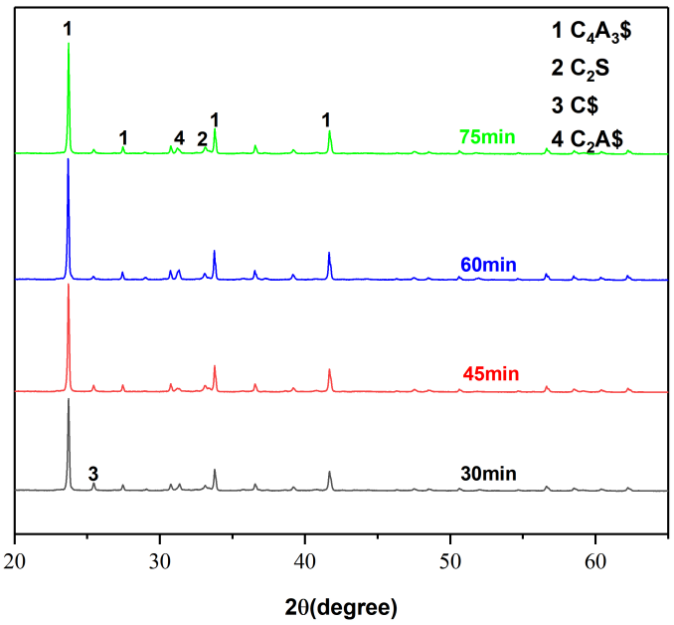

Figure 12. XRD patterns of S2 samples at different times.

Table 7 shows the content of each mineral in the S2 samples for different calcination times. It can be seen that the D1 group contains less $C_4A_3\overline{S}$, and the other three groups have similar $C_4A_3\overline{S}$ content in the clinker with no significant changes. At 75 min, there is a tendency for the $C_4A_3\overline{S}$ to decrease slightly. At the same time, a CA of 3.88% occurs, indicating that the calcination time of the clinker should not be too short, but when the calcination time is too long, a small amount of decomposition of the $C_4A_3\overline{S}$ in the clinker will also occur.

Table 7. Contents of S2 samples fired at different times (wt.%).

Sample	Phase Content (wt.%)						R_{wp} (%)
	$C_4A_3\overline{S}$	C_2S	C_4AF	$C\overline{S}$	C_2AS	CA	
D1	69.01	13.30	5.08	6.50	6.11	-	12.65
D2	72.78	14.52	5.68	3.77	3.25	-	11.17
D3	73.14	15.24	5.77	3.79	-	2.06	13.34
D4	72.24	15.71	5.49	2.68	-	3.88	10.38

The effect of different calcination times on the compressive strength of the cement is shown in Figure 13. The lowest cement compressive strength is evident at a calcination time of 30 min; samples calcined for 45, 60, and 75 min show essentially similar cement compressive strengths with no significant difference, thus further validating the results of the XRD pattern and quantitative analysis, indicating that the clinker minerals formed mainly within 45 min of calcination at high temperatures, with no significant change in strength when extended to 75 min. Therefore, the clinker mineral formation and cement compressive strength results indicate that the optimum holding time for cement clinker calcination is 45 min.

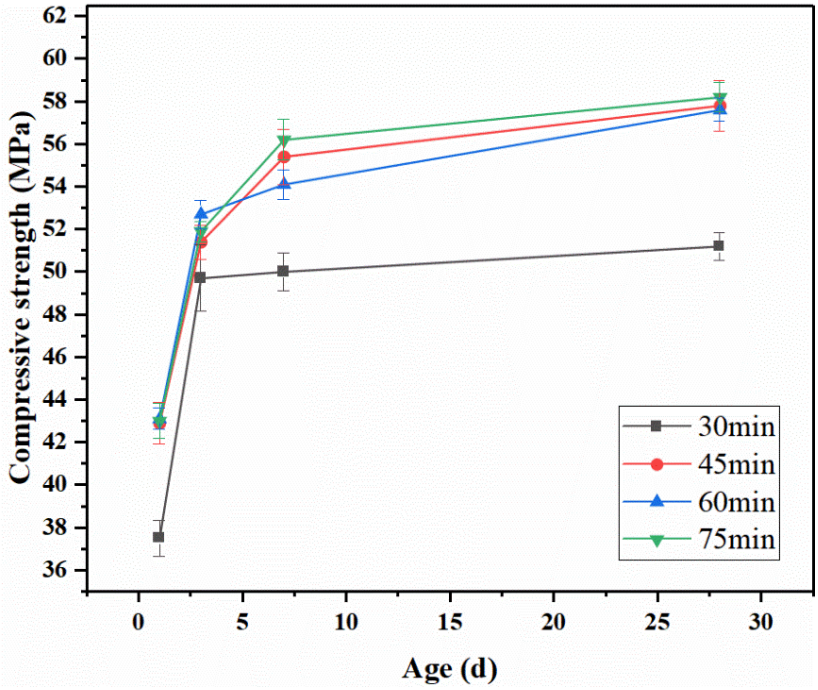

Figure 13. Compressive strength of cement with different calcination times.

4. Conclusions

This study focused on the preparation process and properties of CAS prepared from PG; investigated the control of firing process parameters of CAS clinker; analyzed the influence of raw material ratio, calcination temperature, and time on the mineral type and content of clinker; and established the dosage scheme and firing process model of CAS clinker with PG as the main raw material. The main conclusions are shown below.

(1) The optimum ratio for preparing CAS clinker in this experiment was 42.23% limestone, 17.43% PG, and 40.34% bauxite. The compressive strength of CAS specimens at 1, 3, and 28 days could reach 42.8, 55.5, and 60.9 MPa, respectively.

(2) The optimum process parameter for preparing CAS using PG is calcination at 1250 °C for 45 min. Below 1200 °C, $C_4A_3\overline{S}$ is not yet fully formed, and many transitional phases of C_2AS and $C\overline{S}$ are still present in the clinker. As the calcination temperature increases, the amount of $C_4A_3\overline{S}$ produced gradually increases. At temperatures above 1300 °C, the decomposition of $C_4A_3\overline{S}$ leads to the formation of $C_{12}A_7$ and CA.

(3) The clinker mineral $C_4A_3\overline{S}$ is in the form of round grains and hexagonal plates with a crystal size of 1 to 2 μm, which is relatively tiny and favors the hydration of $C_4A_3\overline{S}$. Calcination temperatures above 1300 °C can affect the particle morphology of $C_4A_3\overline{S}$, changing it from a well-defined polygonal structure to a molten state.

Further studies on the doping behavior of PG in the preparation of P and F elements are needed. In addition, only the compressive strength of the prepared CAS was investigated in this paper; work on other working properties (solidification time, bulk stability, etc.) will follow.

Author Contributions: Conceptualization, J.C. and P.Z.; Methodology, J.C.; Software, B.Z.; Validation, P.Z., B.Z., and J.C.; Formal analysis, B.Z.; Investigation, T.W.; Resources, L.L.; Data curation, J.Z.; L.L.; Writing—original draft preparation, P.Z.; Writing—review and editing, J.C.; B.Z.; Visualization, J.Z.; Supervision, J.C.; B.Z.; Funding acquisition, J.C.; P.Z. All authors have read and agreed to the published version of the manuscript.

Funding: This work was supported by the Natural Science Foundation of Guizhou Provincial Department of Education (Guizhou cooperation KY word (2021) 301), the National Natural Science Foundation of China (52172015), and the Fundamental Research Funds for the Central Universities in China (DUT21ZD201).

Institutional Review Board Statement: Not applicable.

Informed Consent Statement: Not applicable.

Data Availability Statement: Not applicable.

Acknowledgments: This work was supported by the Natural Science Foundation of Guizhou Provincial Department of Education (Guizhou cooperation KY word (2021) 301), the National Natural Science Foundation of China (52172015), and the Fundamental Research Funds for the Central Universities in China (DUT21ZD201). The authors would like to thank Kai Cui from the Dalian University of Technology and The City University of Hong Kong for his contributions to the paper.

Conflicts of Interest: The authors declare no conflict of interest.

References

1. Papastefanou, C.; Stoulos, S.; Ioannidou, A.; Manolopoulou, M. The application of phosphogypsum in agriculture and the radiological impact. *J. Environ. Radioact.* **2006**, *89*, 188–198. [CrossRef] [PubMed]
2. Papaslioti, E.; Pérez-López, R.; Parviainen, A.; Sarmiento, A.M.; Nieto, J.M.; Marchesi, C.; Delgado-Huertas, A.; Garrido, C.J. Effects of seawater mixing on the mobility of trace elements in acid phosphogypsum leachates. *Mar. Pollut. Bull.* **2018**, *127*, 695–703. [CrossRef] [PubMed]
3. Cuadri, A.A.; Pérez-Moreno, S.; Altamar, C.L.; Navarro, F.J.; Bolívar, J.P. Phosphogypsum as additive for foamed bitumen manufacturing used in asphalt paving. *J. Clean. Prod.* **2021**, *283*, 124661. [CrossRef]
4. Ma, B.; Lu, W.; Su, Y.; Li, Y.; Gao, C.; He, X. Synthesis of α-hemihydrate gypsum from cleaner phosphogypsum. *J. Clean. Prod.* **2018**, *195*, 396–405. [CrossRef]
5. Rosales, J.; Pérez, S.M.; Cabrera, M.; Gázquez, M.J.; Bolivar, J.P.; de Brito, J.; Agrela, F. Treated phosphogypsum as an alternative set regulator and mineral addition in cement production. *J. Clean. Prod.* **2020**, *244*, 118752. [CrossRef]
6. Kandil, A.T.; Cheira, M.F.; Gado, H.S.; Soliman, M.H.; Akl, H.M. Ammonium sulfate preparation from phosphogypsum waste. *J. Radiat. Res. Appl. Sci.* **2017**, *10*, 24–33. [CrossRef]
7. Pérez-López, R.; Nieto, J.M.; López-Coto, I.; Aguado, J.L.; Bolívar, J.P.; Santisteban, M. Dynamics of contaminants in phosphogypsum of the fertilizer industry of Huelva (SW Spain): From phosphate rock ore to the environment. *Appl. Geochem.* **2010**, *25*, 705–715. [CrossRef]

8. Kadirova, Z.C.; Hojamberdiev, M.; Bo, L.; Hojiyev, R.; Okada, K. Ion uptake properties of low-cost inorganic sorption materials in the $CaO–Al_2O_3–SiO_2$ system prepared from phosphogypsum and kaolin. *J. Clean. Prod.* **2014**, *83*, 483–490. [CrossRef]
9. Zhang, L.; Su, M.; Wang, Y. Development of the use of sulfo- and ferroaluminate cements in China. *Adv. Cem. Res.* **1999**, *11*, 15–21. [CrossRef]
10. Xin, C.; Jun, C.; Lingchao, L.; Futian, L.; Bing, T. Study on the hydration of Ba-bearing calcium sulphoaluminate in the presence of gypsum. *Cem. Concr. Res.* **2004**, *34*, 2009–2013. [CrossRef]
11. Jun, C.; Jixin, Z.; Yanchen, Y.; Kai, C. Effect of iron phase on calcination and properties of barium calcium sulfoaluminate cement. *Materials* **2021**, *14*, 5813.
12. Gartner, E.M.; Macphee, D.E. A physico-chemical basis for novel cementitious binders. *Cem. Concr. Res.* **2011**, *41*, 736–749. [CrossRef]
13. Gartner, E. Industrially interesting approaches to "low-CO_2" cements. *Cem. Concr. Res.* **2004**, *34*, 1489–1498. [CrossRef]
14. Hao, Y.; Yang, G.; Liang, K. Development of fly ash and slag based high-strength alkali-activated foam concrete. *Cem. Concr. Compos.* **2022**, *128*, 104447. [CrossRef]
15. Péra, J.; Ambroise, J. New applications of calcium sulfoaluminate cement. *Cem. Concr. Res.* **2004**, *34*, 671–676. [CrossRef]
16. Glasser, F.P.; Zhang, L. High-performance cement matrices based on calcium sulfoaluminate–belite compositions. *Cem. Concr. Res.* **2001**, *31*, 1881–1886. [CrossRef]
17. Li, L.; Zhang, Y.; Shi, Y.; Xue, Z.; Cao, M. Surface cracking and fractal characteristics of cement paste after exposure to high temperatures. *Fractal Fract.* **2022**, *6*, 465. [CrossRef]
18. Ludwig, H.; Zhang, W. Research review of cement clinker chemistry. *Cem. Concr. Res.* **2015**, *78*, 24–37. [CrossRef]
19. Cui, K.; Chang, J.; Feo, L.; Chow, C.L.; Lau, D. Developments and applications of carbon nanotube reinforced Cement-Based composites as functional building materials. *Front. Mater.* **2022**, *9*, 146. [CrossRef]
20. Li, J.; Chang, J.; Wang, T.; Zeng, T.; Li, J.; Zhang, J. Effects of phosphogypsum on hydration properties and strength of calcium aluminate cement. *Constr. Build. Mater.* **2022**, *347*, 128398. [CrossRef]
21. Chang, J.; Yu, X.; Shang, X.; Zhao, J.; Zhang, Y. A reaction range for hydration of calcium sulfoaluminate with calcium sulfate and calcium hydroxide: Theory and experimental validation. *Adv. Cem. Res.* **2016**, *28*, 664–674. [CrossRef]
22. Cui, K.; Liang, K.; Chang, J.; Lau, D. Investigation of the macro performance, mechanism, and durability of multiscale steel fiber reinforced low-carbon ecological UHPC. *Constr. Build. Mater.* **2022**, *327*, 126921. [CrossRef]
23. Cuadri, A.A.; Navarro, F.J.; García-Morales, M.; Bolívar, J.P. Valorization of phosphogypsum waste as asphaltic bitumen modifier. *J. Hazard. Mater.* **2014**, *279*, 11–16. [CrossRef]
24. Rashad, A.M. Phosphogypsum as a construction material. *J. Clean. Prod.* **2017**, *166*, 732–743. [CrossRef]
25. Shen, Y.; Qian, J.; Huang, Y.; Yang, D. Synthesis of belite sulfoaluminate-ternesite cements with phosphogypsum. *Cem. Concr. Compos.* **2015**, *63*, 67–75. [CrossRef]
26. Huang, Y.; Qian, J.; Kang, X.; Yu, J.; Fan, Y.; Dang, Y.; Zhang, W.; Wang, S. Belite-calcium sulfoaluminate cement prepared with phosphogypsum: Influence of P_2O_5 and F on the clinker formation and cement performances. *Constr. Build. Mater.* **2019**, *203*, 432–442. [CrossRef]
27. Zhao, J.; Huang, J.; Yu, C.; Cui, C.; Chang, J. Phosphorus substitution preference in ye'elimite: Experiments and density functional theory simulations. *Materials* **2021**, *14*, 5874. [CrossRef] [PubMed]
28. Huang, Y.; Qian, J.; Liu, C.; Liu, N.; Shen, Y.; Ma, Y.; Sun, H.; Fan, Y. Influence of phosphorus impurities on the performances of calcium sulfoaluminate cement. *Constr. Build. Mater.* **2017**, *149*, 37–44. [CrossRef]
29. Shen, Y.; Qian, J.; Chai, J.; Fan, Y. Calcium sulphoaluminate cements made with phosphogypsum: Production issues and material properties. *Cem. Concr. Compos.* **2014**, *48*, 67–74. [CrossRef]
30. Huang, Y.; Qian, J.; Lu, L.; Zhang, W.; Wang, S.; Wang, W.; Cheng, X. Phosphogypsum as a component of calcium sulfoaluminate cement: Hazardous elements immobilization, radioactivity and performances. *J. Clean. Prod.* **2020**, *248*, 119287. [CrossRef]
31. Cui, K.; Chang, J. Hydration, reinforcing mechanism, and macro performance of multi-layer graphene-modified cement composites. *J. Build. Eng.* **2022**, *57*, 104880. [CrossRef]
32. Le Saoût, G.; Kocaba, V.; Scrivener, K. Application of the Rietveld method to the analysis of anhydrous cement. *Cem. Concr. Res.* **2011**, *41*, 133–148. [CrossRef]
33. álvarez-Pinazo, G.; Cuesta, A.; García-Maté, M.; Santacruz, I.; Losilla, E.R.; la Torre, A.G.D.; León-Reina, L.; Aranda, M.A.G. Rietveld quantitative phase analysis of Yeelimite-containing cements. *Cem. Concr. Res.* **2012**, *42*, 960–971. [CrossRef]
34. Cui, K.; Lau, D.; Zhang, Y.; Chang, J. Mechanical properties and mechanism of nano-$CaCO_3$ enhanced sulphoaluminate cement-based reactive powder concrete. *Constr. Build. Mater.* **2021**, *309*, 125099. [CrossRef]
35. Mejdi, M.; Wilson, W.; Saillio, M.; Chaussadent, T.; Divet, L.; Tagnit-Hamou, A. Quantifying glass powder reaction in blended-cement pastes with the Rietveld-PONKCS method. *Cem. Concr. Res.* **2020**, *130*, 105999. [CrossRef]
36. Chang, J.; Cui, K.; Zhang, Y. Effect of hybrid steel fibers on the mechanical performances and microstructure of sulphoaluminate cement-based reactive powder concrete. *Constr. Build. Mater.* **2020**, *261*, 120502. [CrossRef]
37. Xue, W.; Liu, X.; Jing, W.; Yao, Z.; Gao, C.; Li, H. Experimental study and mechanism analysis of permeability sensitivity of mechanically damaged concrete to confining pressure. *Cem. Concr. Res.* **2020**, *134*, 106073. [CrossRef]
38. Huang, Y.; Qian, J.; Liang, J.; Liu, N.; Li, F.; Shen, Y. Characterization and calorimetric study of early-age hydration behaviors of synthetic ye'elimite doped with the impurities in phosphogypsum. *J. Therm. Anal. Calorim.* **2016**, *123*, 1545–1553. [CrossRef]

39. Wu, S.; Yao, Y.; Yao, X.; Ren, C.; Li, J.; Xu, D.; Wang, W. Co-preparation of calcium sulfoaluminate cement and sulfuric acid through mass utilization of industrial by-product gypsum. *J. Clean. Prod.* **2020**, *265*, 121801. [CrossRef]
40. Isteri, V.; Ohenoja, K.; Hanein, T.; Kinoshita, H.; Kletti, H.; Rößler, C.; Tanskanen, P.; Illikainen, M.; Fabritius, T. Ferritic calcium sulfoaluminate belite cement from metallurgical industry residues and phosphogypsum: Clinker production, scale-up, and microstructural characterisation. *Cem. Concr. Res.* **2022**, *154*, 106715. [CrossRef]
41. Li, J.; Chang, J. Effect of crystal/amorphous ratio on mechanical properties in a $C_4A_3\$$-C_2S hydration system with or without gypsum addition. *Constr. Build. Mater.* **2019**, *208*, 36–45. [CrossRef]
42. Zhang, H.; Li, J.; Kang, F. Real-time monitoring of humidity inside concrete structures utilizing embedded smart aggregates. *Constr. Build. Mater.* **2022**, *331*, 127317. [CrossRef]
43. Zhang, H.; Li, J.; Kang, F.; Zhang, J. Monitoring and evaluation of the repair quality of concrete cracks using piezoelectric smart aggregates. *Constr. Build. Mater.* **2022**, *317*, 125775. [CrossRef]
44. Winnefeld, F.; Barlag, S. Calorimetric and thermogravimetric study on the influence of calcium sulfate on the hydration of ye'elimite. *J. Therm. Anal. Calorim.* **2009**, *101*, 949–957. [CrossRef]